

## Wave gradiometry for USArray: Rayleigh waves

Chuntao Liang<sup>1</sup> and Charles A. Langston<sup>1</sup>

Received 7 July 2008; revised 30 November 2008; accepted 15 December 2008; published 18 February 2009.

[1] Wave gradiometry (WG) is a new array data processing technique to extract phase velocity, wave directionality, geometrical spreading, and radiation pattern from spatial gradients of waveforms. A weighted inversion method and a reducing velocity method are introduced to compute spatial gradients accurately for irregular arrays. Numerical experiments are conducted to test techniques and to evaluate the parameters determined from the WG method. We apply this method to USArray data for the western United States. In this study, Rayleigh waves from nine earthquakes with varying azimuths are analyzed. The stability of this method is shown by the similarity between the results from two nearly collocated earthquakes from the Kurile Islands. The error check shows the WG results are stable for ambient noise level as high as 10%. Phase velocities determined by WG and two station (TS) methods are statistically consistent, while these determined from beam forming method are systematically higher for wavelength larger than one quarter of the array diameter. Our results show that, first, the average phase velocities of Rayleigh waves range from 3.8 to 4.1 km/s for periods from 60 s to 150 s. This is consistent with average earth models. The prominent feature on the phase velocity map is that the Basin and Range province is dominated by velocity lows while the west coast of the United States and the north and northeastern Snake River plain are dominated by velocity highs. The Snake River plain appears to be a primary tectonic boundary. Second, azimuthal variations represent the accumulated wave directionality changes along the raypath. A velocity contrast of 0.25 km/s across the oceanic-continental lithosphere boundary along the west coast of the United States is needed to explain the negative azimuth variations. Third, geometrical spreading is slightly anticorrelated with phase velocity, which may suggest that amplitude variations in radial directions are subject to surface wave focusing and defocusing. Fourth, similar to the wave directionality, radiation pattern variations also exhibit strong path dependence. Further theoretical and experimental studies will be conducted to understand the two amplitude parameters: geometrical spreading and radiation pattern and their relations with the local geophysical properties.

**Citation:** Liang, C., and C. A. Langston (2009), Wave gradiometry for USArray: Rayleigh waves, *J. Geophys. Res.*, 114, B02308, doi:10.1029/2008JB005918.

### 1. Introduction

[2] Seismic arrays are deployed globally, regionally, or locally to record seismic waves for source mechanism or Earth structure studies. One of the best recent examples of a regional array is the transportable component of the USArray that consists of 400 stations deployed in a nearly uniform grid. With an average spacing of 70 km, this rolling array has been providing invaluable seismic data to study the structure and evolution of the North American continent. Figure 1 shows a snapshot of the USArray on 13 January 2007. Data sets from USArray are being used in many traditional techniques, such as body and surface wave travel

time tomography [Sigloch and Nolet, 2007; Yang and Ritzwoller, 2008; Beghein et al., 2007], waveform tomography [Bedle and van der Lee, 2007], receiver function analysis [Levander et al., 2007], shear wave splitting [West, 2007] and the recently emerging ambient noise tomography technique [Lin et al., 2008; Moschetti and Ritzwoller, 2007].

[3] Most existing seismic processing methods in earthquake seismology, such as travel time tomography, waveform tomography, receiver function, and shear wave splitting, treat each element in the array as a point measurement. Therefore, measurements from isolated receivers often reflect the accumulated effects of the media along the whole raypath from the seismic source. Also, travel times are often the most important measurements for many techniques, such as in travel time tomography, receiver function, and shear wave splitting, but amplitudes are rarely taken into account or are secondary to the analysis. The beamforming method [Birtill and Whiteway, 1965; Rost and

<sup>1</sup>Center for Earthquake Research and Information, University of Memphis, Memphis, Tennessee, USA.

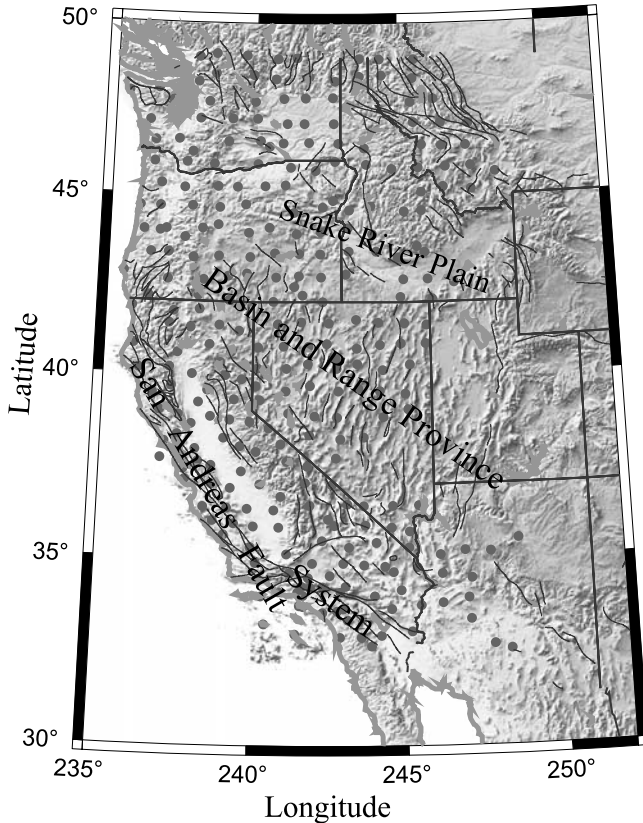


**Figure 1.** A snapshot of the USArray station coverage (dots) plotted on top of the topography of the western United States. The thin and thick lines are major faults and state boundaries, respectively. Station coverage only represents the USArray on 13 January 2007. Waveforms recorded on these stations from the Kurile Island earthquakes on this day are analyzed in great details in this study.

Thomas, 2002] and two-station phase velocity measurement method [Knopoff *et al.*, 1966; Yao *et al.*, 2006] are two popular array processing techniques, but the wave amplitude information is removed due to waveform summation or cross-correlation.

[4] The wave gradiometry (WG) method, on the other hand, is a new array data processing technique to extract phase velocity, wave directionality, geometrical spreading, and radiation pattern from spatial gradients of waveform amplitudes. The spatial gradients of wave amplitudes can be explicitly related to physical properties of Earth's continuum, such as strain and stress [Langston, 2007a]. The spatial gradients of a wavefield are directly related to wave amplitude and its time derivative [Langston, 2007a]. WG has been applied to extract wave slowness and geometrical spreading for a 1-D linear array [Langston, 2007a]. Applied to a 2-D array, radiation pattern and wave directionality are two more parameters that can be extracted by this method [Langston, 2007b]. This method can be applied to any part of the wavefield including body waves and surface waves. In this study, we applied the WG method to the surface waves recorded by USArray (Figure 1).

[5] As a new technique, the strengths and limitations as well as some theoretical issues of WG remain to be

explored. Major issues include how to compute wave gradients for irregular seismic arrays; how medium heterogeneity, ambient noise, and wave interference affect WG results; how WG results compare to other array techniques such as the beam-forming and two-station methods; and how the WG parameters can be used to solve tectonic problems.

[6] Several different techniques exist to analyze surface waves. First, the whole waveform may be modeled to solve for a 1-D structure along the raypath, and then the 1-D structures along different paths are combined to form a 3-D image using waveform tomography [van der Lee and Nolet, 1997; van der Lee and Frederiksen, 2005]; second, the timing of the waveform envelope peak may be measured to find group velocity [Herrmann, 1973; Barmin *et al.*, 2001; Liang and Langston, 2008a]; third, the relative waveform peak moveout between two stations aligned along the raypath is measured to find the phase velocity [Knopoff *et al.*, 1966; Yao *et al.*, 2006]; and fourth, Forsyth and Li [2005] as well as Yang and Ritzwoller [2008] used two-plane wave method to solve phase velocity variation across an array and wave direction deviation simultaneously. The measurements of the first two methods reflect the media along the whole path and are often complicated by the source and the structure outside of the region covered by an array. The third method (two station method) also yields phase velocity, but it requires that the two stations are aligned along the raypath. Therefore, earthquakes from a wide range of azimuths are required to provide crossing paths to improve coverage. Furthermore, amplitudes are not taken into account in this method. The fourth method yields both phase velocity and wave direction deviation from great circle path, but directions are assumed constant for the entire array. On the other hand, the WG method yields local phase velocity maps that span the whole array based on waveforms. In addition, it provides wave directionality and amplitude variation in radial and transverse directions for every station. This extra information is very useful for the study of wave scattering, attenuation, and anisotropy.

[7] The theory of WG had been introduced in a series of papers by Langston [2007a, 2007b, 2007c] and Langston and Liang [2008]. For the convenience of discussion, some basic equations are reviewed as follows.

[8] In a Cartesian coordinate system, the wave function of a displacement, velocity, or acceleration at location  $(x, y)$  may be written as:

$$u(x, y) = G(x, y)f(t - xp_x - yp_y), \quad (1)$$

where  $G(x, y)$  represents the amplitude variation across space;  $f(t, x, y)$  represents the phase variation as a function of time  $t$  and location  $(x, y)$  with  $p_x$  and  $p_y$  the slowness in the  $x$  and  $y$  direction, respectively. Taking derivatives of the equation (1) with respect to  $x$  and  $y$ , respectively, gives:

$$\frac{\partial u(t, x, y)}{\partial x} = A_x u(t, x, y) - p_x \frac{\partial u(t, x, y)}{\partial t}, \quad (2)$$

and

$$\frac{\partial u(t, x, y)}{\partial y} = A_y u(t, x, y) - p_y \frac{\partial u(t, x, y)}{\partial t}, \quad (3)$$

where  $A_x(x, y) = \frac{\partial G}{\partial x} \frac{1}{G}$  and  $A_y(x, y) = \frac{\partial G}{\partial y} \frac{1}{G}$  are the normalized spatial gradients of the wave amplitudes in the  $x$  and  $y$  directions, respectively. Here we have assumed that  $p_x$  and  $p_y$  are not changing across a small subarray that is used to compute the spatial gradients as discussed in the section 2 and 3.

[9] In section 2.1, we introduce a weighted inversion method and a reducing velocity method to compute the spatial gradients. With the waveform  $u$ , its temporal derivative and spatial gradients known, A frequency domain method [Langston, 2007b] or a time domain method [Langston, 2007c] may be used to extract  $A_x(x, y)$ ,  $A_y(x, y)$ ,  $p_x$  and  $p_y$  from equation (2) and (3). The time domain method is used in this study because it is more stable by avoiding spectral division that may cause numerical instabilities for small spectrum amplitudes. The time domain method involves applying Hilbert transform to equation (2) and identifying real and imaginary parts to find  $A_x(x, y)$  and  $p_x$ . Working the same way on equation (3) we can find  $A_y(x, y)$  and  $p_y$ .

[10] Once  $A_x(x, y)$ ,  $A_y(x, y)$ ,  $p_x$  and  $p_y$  are found, by transforming from Cartesian to cylindrical coordinates, the following relations may be obtained to find the slowness  $p$ , wave azimuth  $\theta$ , radiation pattern  $A_\theta$ , and geometrical spreading  $A_r$  [Langston, 2007b]:

$$p = \sqrt{p_x^2 + p_y^2}, \quad (4)$$

$$\theta = \tan^{-1} \left( \frac{p_x}{p_y} \right), \quad (5)$$

$$A_\theta(\theta) = \frac{\partial G}{\partial \theta} \frac{1}{G} = r(A_x \cos(\theta) - A_y \sin(\theta)), \quad (6)$$

$$A_r(\theta) = \frac{\partial G}{\partial r} \frac{1}{G} = A_x \sin(\theta) - A_y \cos(\theta), \quad (7)$$

where  $r$  is the epicentral distance. The phase velocity can be found by:

$$v = \frac{1}{p}. \quad (8)$$

This technique has been successfully applied to a linear accelerometer array [Langston et al., 2006], a minigegophone array [CERI Array Working Group, 2007], and a local broadband seismometer array [Langston, 2007b; Langston and Liang, 2008]. In this paper, we report the application of this technique to the USArray, a regional array with nearly uniform station distribution.

## 2. Methodology

### 2.1. Computing Wave Gradients

#### 2.1.1. Inversion Method

[11] To find the four wave gradiometry parameters, the very first and the most important step is to find the spatial gradients. For a regularly spaced array or array with minor irregularity, a finite difference method or weighted finite

difference method may be applied to compute spatial gradients [Langston, 2007a]. An inversion method was applied for an array with arbitrary geometry [Spudich et al., 1995]. In this study, we propose a weighted inversion method to compute wave gradients for an array with any geometry.

[12] Consider a small array as shown in Figure 2. The wave functions at receivers  $s_i$ ,  $i = 0, 1, 2, \dots, N$  are  $u_i$ , respectively. On the basis of the Taylor series, the spatial gradients at the master receiver  $s_0$  can be related to the wave functions at all other receivers as:

$$du_i = u_i - u_0 = \delta x_i \frac{\partial u}{\partial x} \Big|_{s_0} + \delta y_i \frac{\partial u}{\partial y} \Big|_{s_0} + du_i^{err}, \quad (9)$$

with  $\delta x = x_i - x_0$  and  $\delta y = y_i - y_0$ . Under the assumption that the second orders of the wavefield are not changing dramatically within a subarray, the truncation errors satisfy:

$$du_i^{err} \leq \delta x_i^2 \frac{\partial u^2}{2\partial^2 x} \Big|_{s_0} + \delta y_i^2 \frac{\partial u^2}{2\partial^2 y} \Big|_{s_0} + \delta x \delta y \frac{\partial u^2}{\partial x \partial y} \Big|_{s_0}, \quad (10)$$

Taking the first order approximation of equation (9), we have

$$du_i \cong \delta x_i \frac{\partial u}{\partial x} \Big|_{s_0} + \delta y_i \frac{\partial u}{\partial y} \Big|_{s_0}. \quad (11)$$

Equation (11) can be written in a matrix form as:

$$\begin{bmatrix} u_1 - u_0 \\ u_2 - u_0 \\ \vdots \\ u_N - u_0 \end{bmatrix} = \begin{bmatrix} \delta x_1 & \delta y_1 \\ \delta x_2 & \delta y_2 \\ \vdots & \vdots \\ \delta x_N & \delta y_N \end{bmatrix} \begin{bmatrix} \partial u / \partial x \\ \partial u / \partial y \end{bmatrix}, \quad (12)$$

where the  $N >= 2$  denotes the number of supporting receivers. For simplicity, equation (12) may be written as:

$$\mathbf{d} = \mathbf{C}\mathbf{g}, \quad (13)$$

where  $\mathbf{d}$ ,  $\mathbf{C}$ , and  $\mathbf{g}$  are the data matrix (waveform variations with respect to the master station), the array geometry matrix, and the spatial gradients, respectively. The spatial gradients  $\mathbf{g}$  may be found by simply solving the equation system (13).

#### 2.1.2. Weighted Inversion Method

[13] The linear equation system (13) is, however, based on the first-order Taylor series approximation and the truncation errors due to the higher orders are not taken into account. To estimate the truncation error term  $du_i^{err}$  similar to the 1-D case in the work of Langston [2007a], we assume a sinusoidal wave with a frequency  $\omega$  for the error equation (10) and obtain the truncation error rates as:

$$\left| \frac{du_i^{err}}{du_i} \right| \leq \frac{1}{2} \omega (p_x \delta x_i + p_y \delta y_i). \quad (14)$$

This equation indicates that the truncation errors are proportional to the wave phase delay or advance between the station  $s_0$  and  $s_i$  as well as the frequency  $\omega$ . That is, for

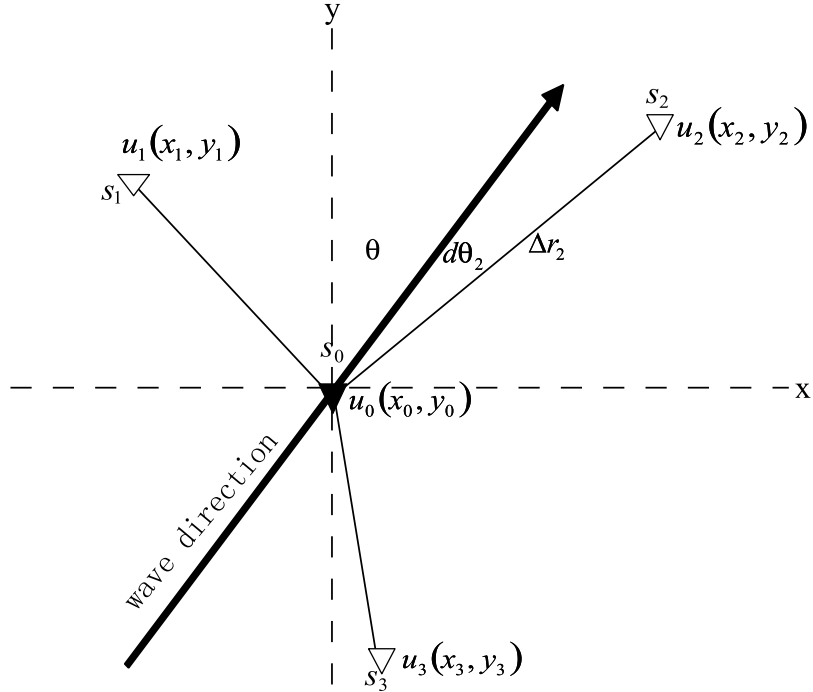


**Figure 2.** An irregular array for wave gradiometry. The receiver in the center ( $s_0$ ) is called master receiver while other receivers ( $s_i$ ,  $i = 1, 2, 3$ ) are called supporting receivers. The thick black line denotes a raypath passing by the master receiver. Here  $\theta$  is the back azimuth of the ray while  $d\theta_2$  is the angle between the raypath and the line connecting receiver 2 and the master receiver.

the given array, the lower the frequency, the smaller the truncation errors.

[14] For a wave (surface or body wave) propagating in the direction  $\vec{R}$  with azimuth  $\theta$  (Figure 2) and a slowness  $p$ , its two horizontal components are  $p_x = p \sin(\theta)$  and  $p_y = \cos(\theta)$ . Supposing that the angle between the wave vector  $\vec{R}$  and the station pair vector (pointing from the  $s_0$  to  $s_i$ ) is  $d\theta_i$ . It is straight forward to find that  $\delta x_i = \delta r_i \sin(\theta + d\theta_i)$  and  $\delta y_i = \delta r_i \cos(\theta + d\theta_i)$ . Substituting these relations into the equation (14) and manipulating it a little, we obtain:

$$\left| \frac{du_i^{err}}{du_i} \right| \leq \frac{\pi f}{c} \delta r_i \cos(d\theta_i), \quad (15)$$

with  $f$  and  $c$  being the frequency and phase velocity, respectively.

[15] This new relation suggests that errors due to the higher-order truncation are proportional to the wave frequency  $f$  and station spacing  $\delta r$  and inversely proportional to the phase velocity  $c$ . Surprisingly, we find that truncation errors are also dependent on the angles ( $d\theta$ ) between the wave vector and the station pair vectors. For a station pair parallel or perpendicular to the wave vector, i.e.,  $d\theta = 0$  or  $d\theta = 90^\circ$ , the error rates are maximum and minimum, respectively. This relation is best illustrated by the numerical experiments in section 2.1.4. This observation may be used as a criteria for designing arrays for the WG method to work well.

[16] To take the truncation errors into account, we modify the equation system (12) by weighting each datum (i.e., each row) according to the truncation errors. This is equivalent to down-weighting the data with higher truncation

errors and up-weighting the data with smaller errors. The weighting is done by left-multiplying a weighting matrix on both sides of equation (12). The weighting matrix has the form:

$$\mathbf{W} = \begin{bmatrix} w_1 & 0 & \cdots & 0 \\ 0 & w_2 & 0 & 0 \\ \vdots & 0 & \ddots & 0 \\ 0 & 0 & 0 & w_N \end{bmatrix}, \quad (16)$$

where  $w_i$  is the weight for the corresponding receiver pair and it is quantified by

$$w_i = \frac{1}{\left| \frac{\pi f}{c} \delta r_i \cos(d\theta_i) \right| + \varepsilon}, \quad (17)$$

where the  $\varepsilon$  denotes the data errors associated with waveforms and the first term in the denominator denotes errors associated with the geometry. Because waveforms used in this study are very clean, a constant  $\varepsilon = 0.01$  is used mainly to damp the weighting when the errors due to the geometry are too small. A large  $\varepsilon$  may make the errors associated with the geometry less significant.

[17] Applying the weighting matrix, the equation (13) becomes:

$$\mathbf{Wd} = \mathbf{WCg}. \quad (18)$$

Letting  $\mathbf{d}' = \mathbf{Wd}$  and  $\mathbf{C}' = \mathbf{WC}$ , we get:  $\mathbf{d}' = \mathbf{C}'\mathbf{g}$ . The singular value decomposition (SVD) method is then applied

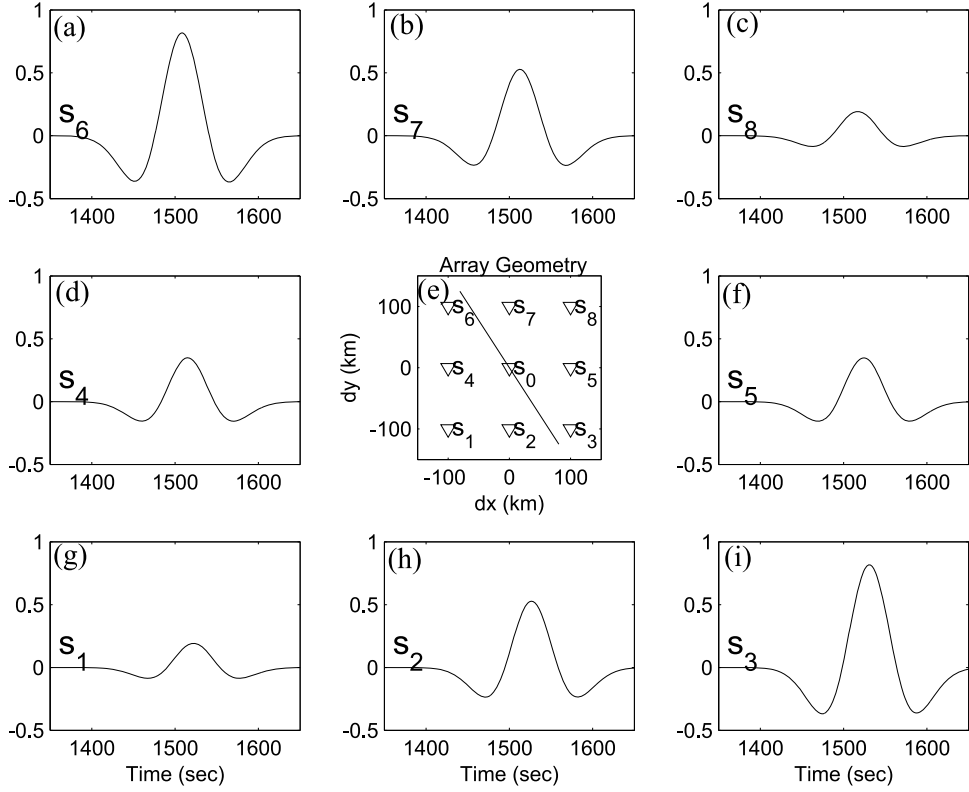


**Figure 3.** Ratio between higher-order truncation errors and the first-order of Gaussian waves. Figure 3e shows the geometry of the array and the straight line shows the direction of the wave. The center of the array is located at (3300 km, -5100 km) with respect to a source at (0 km, 0 km). The master receiver  $s_0$  is surrounded by eight supporting receivers  $s_i$   $i = 1, 2, \dots, 8$ . The other eight windows show the ratio between the truncation errors and the first order for the eight corresponding receivers. See the text for details.

to solve this new equation system to find the spatial gradients  $\mathbf{g}$ .

### 2.1.3. Reducing Velocity Method

[18] Equation (15) suggests that the higher-order truncation errors in the Taylor series are inversely related to the phase velocity. In addition to the weighted inversion method, a reducing velocity method as introduced by *Langston* [2007b] may effectively decrease the truncation errors by intentionally increasing the phase velocity  $c$ . This method assumes that the medium is homogeneous within one subarray and supposes that we know the average phase velocity,  $\bar{c}$ . We may remove the phase shifts due to this average velocity by replacing the  $p_x$  and  $p_y$  with:

$$p'_x = p_x - \bar{p}_x, \quad (19)$$

and

$$p'_y = p_y - \bar{p}_y, \quad (20)$$

respectively, where  $\bar{p}_x = \frac{\sin(\theta)}{\bar{c}}$  and  $\bar{p}_y = \frac{\cos(\theta)}{\bar{c}}$ . This is equivalent to increasing the apparent velocity and thus lowering the truncation errors. Keep in mind though, the average slowness  $\bar{p}_x$  and  $\bar{p}_y$  have to be added back to the slowness obtained from equation (4), i.e.,  $p'_x$  and  $p'_y$ , to get the real phase velocity.

[19] This method is implemented by shifting the waveform of the supporting station  $s_i$  by  $t_i = -\bar{p}_x \delta x_i - \bar{p}_y \delta y_i$  in the time domain. Using this reducing velocity method, the phase moveout between the supporting stations and master station are decreased and thus the spatial gradients will be reduced as shown in the numerical experiments.

### 2.1.4. Numerical Experiments

[20] We conducted a series of numerical experiments to test these methods. Assume the wave function in equation (1) is a Gaussian function (Figures 4a and 4b)

$$u(t, x, y) = \frac{1}{\sqrt{x^2 + y^2}} \exp \left[ -\alpha (t - xp_x - yp_y)^2 \right], \quad (21)$$

where  $\alpha = 0.0005$ . This wave propagates across a  $3 \times 3$  array (Figure 3e) with its central element located at (3300, -5100) km from the source and a uniform spacing of 100 km in both the x and y directions. The synthetic array spacing is comparable to the station spacing of USArray. The distance between the source (0,0) and the array (6075 km) as well as the back azimuth of the synthetic rays ( $147^\circ$ ) are comparable to the epicentral distances and azimuths of seismic rays from Kurile Island earthquake (e.g., Kurile01 in the Table 1) to the USArray.

[21] The synthetic waveforms  $u_0$  and  $u_i$  as well as their theoretical spatial gradients  $\frac{\partial u}{\partial x} \Big|_{s_0}$  and  $\frac{\partial u}{\partial y} \Big|_{s_0}$  (blue lines in

**Table 1.** Events Used in Wave Gradiometry Study

Event	Event Time (year/month/day/hh:mm)	Latitude (°N)	Longitude (°E)	Depth (km)	Mag (Mw)	Location	Station
1	2007/01/13/04:23	46.27	154.45	10	7.9	Kurile01	296
2	2006/11/15/11:14	46.59	153.27	10	8.3	Kurile02	259
3	2006/10/15/17:07	19.88	-155.94	38	6.7	Hawaii	259
4	2007/08/15/23:30	-13.36	-76.52	30.2	8.0	Peru	327
5	2007/04/05/03:56	37.31	-24.62	14	6.2	Azores	260
6	2007/08/01/17:08	-15.65	167.54	172.90	7.2	Vanuatu	356
7	2007/04/01/20:39	-8.41	156.95	10	7.6	Solomon	277
8	2007/09/30/05:23	-49.39	163.84	18.9	7.3	Auckland	389
9	2007/08/04/14:24	-4.8	-105.41	10	5.9	EPR	354

Figures 4a, 4c, and 4d, respectively) are substituted into equation (22) to compute the normalized truncation errors due to higher-order terms of the Taylor series:

$$du_i = \left[ u_i - u_0 - \left( \delta x_i \frac{\partial u}{\partial x} + \delta y_i \frac{\partial u}{\partial y} \right) \right] / \max(du_i). \quad (22)$$

The normalized truncation errors for the eight auxiliary stations ( $s_i$ ,  $i = 1, 2, \dots, 8$ ) are plotted in Figures 3a–3d

and 3f–3i, respectively. Note that all error functions have the shape of a second-order derivative of a Gaussian function. The truncation errors can be as high as 70% of the first-order Taylor series approximation for receivers  $s_3$  and  $s_6$  ( $d\theta_3$  and  $d\theta_6$  are small) while as low as 15% for receivers  $s_1$  and  $s_8$  ( $d\theta_1$  and  $d\theta_8$  are large). This observation is consistent with our error equation (15). The effects of distances between the supporting receivers and the master receiver are not visible because all distances in this case are very close.

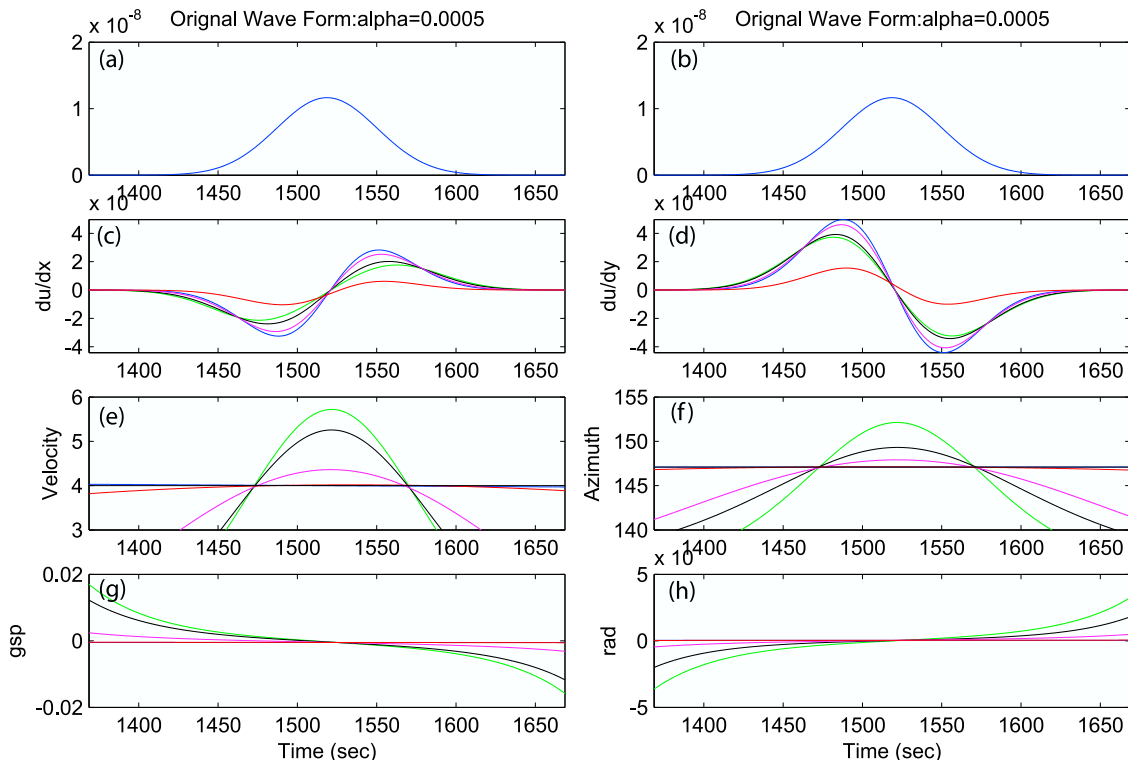


**Figure 4.** Computed spatial gradients and four WG parameters using different methods. (a and b) Gaussian waveforms for reference. (c and d) Computed spatial gradients in the  $x$  and  $y$  directions using different methods, respectively. The blue curves are the theoretical spatial gradients. The other four curves are results using finite difference method (green), inversion without weighting (black), inversion with weighting (magenta), and the inversion with weighting and reducing velocity method (red). (e–h) Computed phase velocity, azimuth, geometrical spreading, and radiation pattern, respectively, using corresponding spatial gradients in Figures 4c and 4d. The horizontal lines in Figures 4e and 4f are the true velocity (4.0 km/s) and true azimuth (147°), respectively. Notice that the blue curves in Figures 4e–4h are indistinguishable from the red curves which means that the WG parameters computed from the combination of both reducing velocity and weighted inversion methods are very close to the theoretical results.

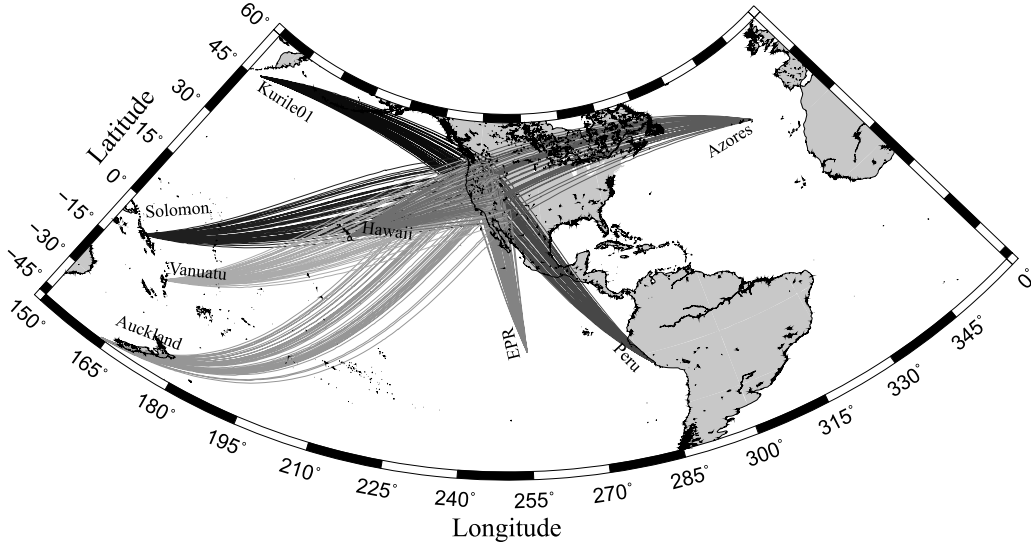


**Figure 5.** Earthquakes used in this study with great circle raypaths. Refer to Table 1 for the parameters of each earthquake. Only 10% the rays are plotted for clarity. EPR is East Pacific Rise. The Kurile02 event in Table 1 is not plotted because it is only about 100 km away from the Kurile01 event.

[22] We now compute the spatial gradients and WG parameters using different methods and compare them to the theoretical results. The four methods compared in the Figure 4 are (1) the finite difference method:  $\frac{\partial u}{\partial x} = \frac{u_1+u_6-u_3-u_8}{4\delta x}$  and  $\frac{\partial u}{\partial y} = \frac{u_1+u_3-u_6-u_8}{4\delta y}$  (green); (2) inversion method without weighting using equation (12) (black); (3) the inversion method with weighting using equation (18) (magenta); and (4) the combination of weighted inversion and reducing velocity method (red). In addition, we also investigated the finite difference method involving all nine stations  $\frac{\partial u}{\partial x} = \frac{u_1+u_4+u_6-u_5-u_8}{6\delta x}$  and  $\frac{\partial u}{\partial y} = \frac{u_1+u_2+u_3-u_6-u_7-u_8}{6\delta y}$  to find the spatial gradients. This method yielded the same results as the inversion method without weighting, thus only the latter is further discussed.

[23] Figure 4 shows each parameter as a time series (even though they are not time series in theory). The computed parameters are closer to the theoretical results at the timing of the waveform peak due to the higher signal-to-noise ratio. The results from the weighted inversion method (magenta) are obviously closer to the theoretical results (blue) than the inversion without weighting and finite difference methods. However, a combination of the weighted inversion and the reducing velocity method (red) is clearly superior to the other three methods. Therefore, both the weighted inversion and the reducing velocity method will be applied in the real data analysis in section 3. Note that the amplitudes of the spatial gradients using the method (4) that involves a reducing velocity are much smaller than the other methods and the theoretical. This is because the reducing velocity is equivalent to reducing the slowness  $p_x$  and  $p_y$  in the equation (1) and thus reducing waveform variations across the array.

### 3. Application to USArray

[24] In this section, we present results from waveforms recorded by USArray from nine earthquakes from different azimuths. The nine earthquakes are listed in Table 1 and

their raypaths are shown in Figure 5. Ideally this method can be applied to any seismic phase. In this paper we concentrate on the Rayleigh waves.

#### 3.1. Data Processing of One Subarray

[25] After downloading waveforms from the IRIS data management center, the following procedure is applied: (1) inspect data to make sure the target phases are clean and strong on all waveforms; (2) remove instrument responses, wave trends, and means; (3) filter waveforms to the target frequency bands; (4) remove stations whose peak amplitudes are about 30% larger or smaller than surrounding stations; and (5) apply the reducing velocity method by shifting waveforms according to an average phase velocity (4 km/s for example) to remove the effects due to the background velocity. Thus the computed phase velocity represents a perturbation with respect to the average velocity  $\bar{c}$ . We then (6) find spatial gradients using equation (18); (7) compute  $A_x$ ,  $A_y$ ,  $p_x$  and  $p_y$  using the technique introduced by Langston [2007c]; (8) take into account the average velocity  $\bar{c}$  and find the true slowness by  $p_x = p'_x + \frac{\sin(\theta)}{\bar{c}}$  and  $p_y = p'_y + \frac{\cos(\theta)}{\bar{c}}$ ; (9) use equations (4)–(8) to compute the four major wave gradiometry (WG) parameters; and then (10) pick the phase velocity at the envelope peak. This new velocity is used as the reducing velocity and the process repeated from step 5 to step 9, until the phase velocity differences  $dv = |v_i - v_{i-1}|$  between the two successive loops are smaller than 0.01 km/s. In practice,  $dv$  decreases to below 0.01 km/s within three iterations for most subarrays.

[26] As an example, we use waveforms from the Kurile Islands earthquake on 13 January 2007 (Kurile01 in Table 1 and Figure 5) recorded on nine stations centered at station P07A to show the basic processing steps. Figure 6a shows the relative location of the subarray and the great circle path. Waveforms for the period band (100–125 s) of this subarray are shown in the Figure 6b with the waveform of the master station highlighted.

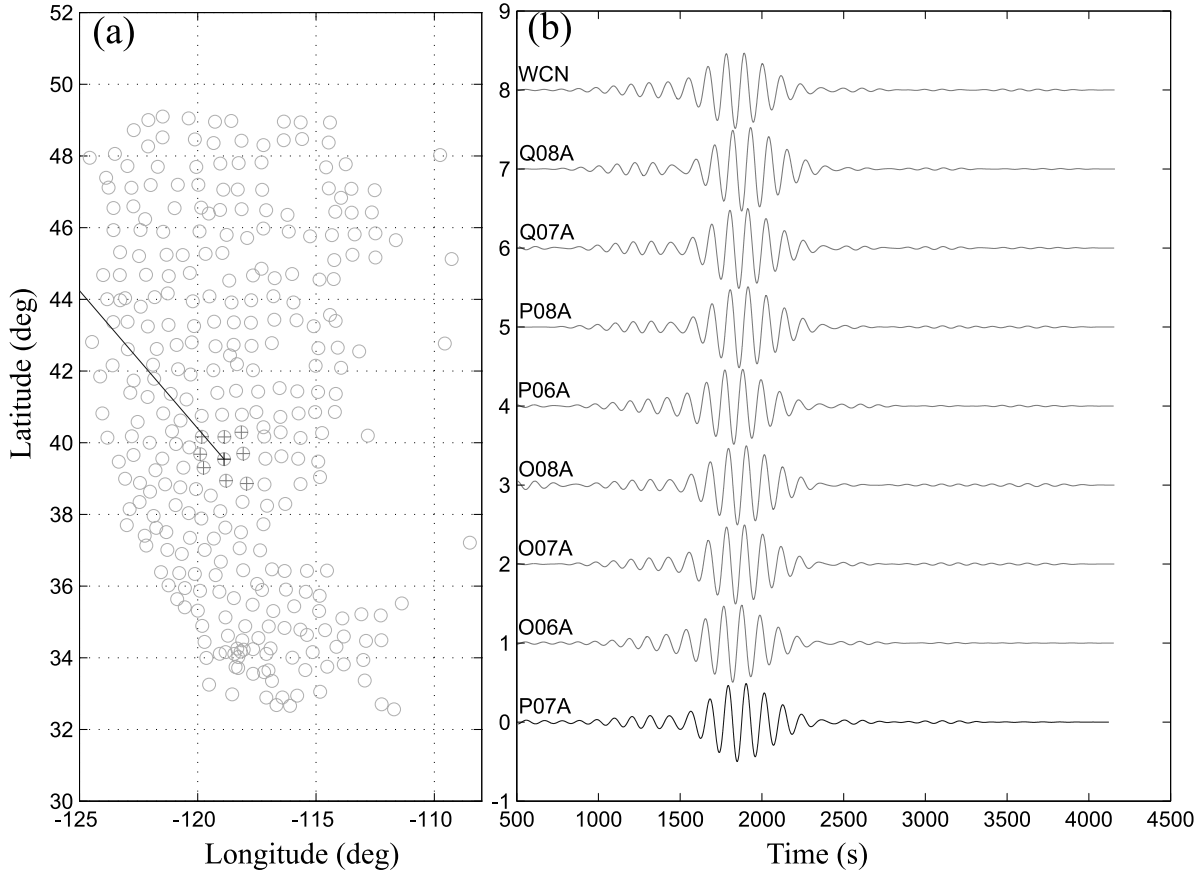


**Figure 6.** Geometry of a subarray with waveforms. (a) Stations (circles) that recorded the Kurile01 earthquake. Pluses are stations of the subarray. The straight line shows the ray direction. (b) Waveforms of the master station P07A (the bottom trace) and supporting stations (other traces) are shown. Station names are annotated.

[27] Fundamental mode Rayleigh waves dominate this period band. The similarity between waveforms is significant but subtle variations are visible. It is the subtle variations that carry the structure information across the subarray. The waveform of the master station and the computed phase velocity ( $c$ ), azimuth variation ( $\delta\theta$ ), geometrical spreading ( $A_r$ ), and radiation pattern ( $A_\theta$ ) are plotted in Figure 7 from top to bottom, respectively. The group velocity of the wave package is about 3.63 km/s. All four WG parameters are relatively stable within the time window (1400–2500 s) of the wave package. Sharp variations are observed at both ends of the time window and are probably due to the interference between different seismic phases [Langston, 2007c]. We then measure the four parameters at the time of the waveform peak (marked by black vertical bars). The standard deviation of each parameter within one period around the wave peak is treated as the measurement error. The phase velocity for the Rayleigh wave is about 3.93 km/s which is close to the global average phase velocity of the fundamental mode Rayleigh waves at this period band based on the PREM model [Dahlen and Tromp, 1998; Dziewonski and Anderson, 1981]. The azimuth perturbation is about  $3^\circ$  with a very small error.

### 3.2. WG Parameter Maps for the Kurile Islands Earthquakes

[28] This procedure is applied to all other stations, and we then average WG parameters within a half wavelength radius to remove the spurious results from localized noise. Figure 8 shows the four maps for the Kurile island earthquake on 13 January 2007 (Kurile01 in Table 1) in the period band of 100–125 s. Figure 9 shows the statistics and corresponding measurement errors in four different period bands (see the caption for details). Note that the errors of velocity are generally less than 0.03 km/s (Figure 9b). The average phase velocity increases with period and is consistent with the theoretical dispersion curve [Dahlen and Tromp, 1998]. Figure 8a shows the phase velocity perturbations with respect to an average velocity of 4.00 km/s (refer to the triangular-marked curve in Figure 9a). The most striking feature on Figure 8a is that the west coast of the United States is dominated by high velocities while the Basin and Range province is characterized by low velocities (refer to the Figure 1 for location names). The Snake River plain is associated with a very low velocity belt. Similarly, low  $P$  wave velocity is observed in the upper mantle beneath the Snake River Plain obtained from  $Pn$  tomography by Hearn [1996]. These observations are consistent

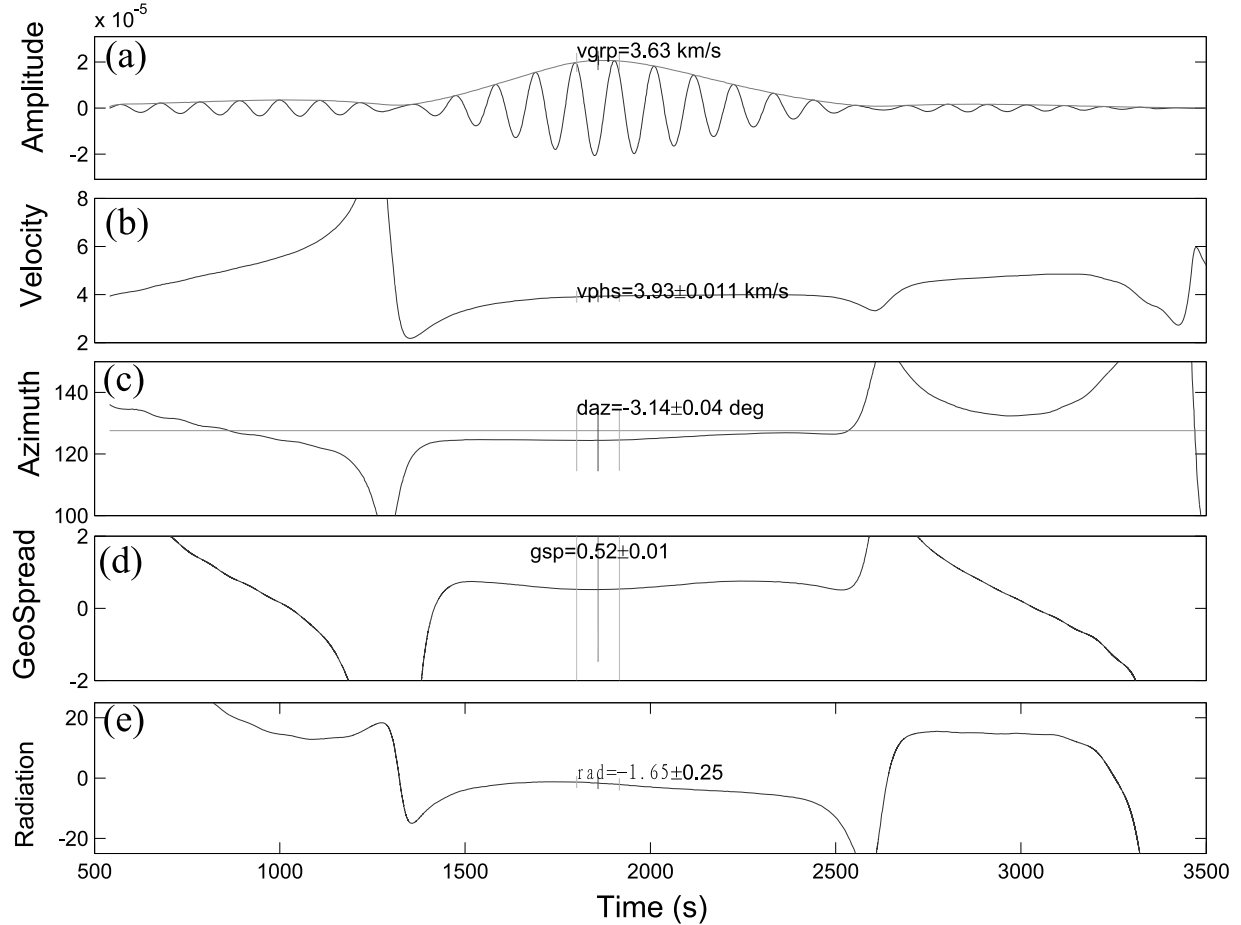


**Figure 7.** Wave gradiometry results for the subarray shown in Figure 6. (a) Waveform of the master station (P07A), (b) phase velocity, (c) back azimuth, (d) geometrical spreading, and (e) radiation pattern. The horizontal line in Figure 7c is the great circle back azimuth. The vertical bar in the middle marks the timing of the waveform peak. The corresponding values at this time are shown beside the bars. The number beside the bar in Figure 7a is group velocity. Another two bars are about half of the period apart from the bar in the middle. The standard deviation between these two times is given as errors for corresponding parameters (second numbers in Figures 7b–7e). On Figures 7b, 7c, 7d, and 7e, the two numbers are the parameter values and the corresponding errors, respectively.

with the hypothesis that the Snake River Plain represents the track of the Yellowstone hot spot [Armstrong *et al.*, 1975; Saltzer and Humphreys, 1997]. The general features observed in this study are also consistent with the velocity map inverted using the two plane wave method with the USArray data set [Yang and Ritzwoller, 2008].

[29] The absolute azimuth variations are generally smaller for longer periods (Figure 9c) with errors less than  $1^\circ$  (Figure 9d). Azimuth variations illustrate strong path direction dependency (Figure 8b). The two belts of negative and positive variations correspond to the two peaks of the triangle-marked curve on Figure 9c. Figure 10 shows both great circle raypaths and the azimuth variations. Note that all rays south of the Aleutian subduction zone have negative azimuth variations, that is, smaller computed back azimuths than great circle back azimuths, with the average change being about  $7^\circ$  (refer to the first peak on the triangular-marked curve on Figure 9c). As we show in the discussion, a velocity contrast of  $0.25 \text{ km/s}$  between the oceanic lithosphere to west and the continental lithosphere to east

is enough to account for such azimuth anomaly. On the other hand, rays passing through the Aleutian subduction zone, except for a small strip east of the Snake River plain, all have positive variations, or, larger computed back azimuths than great circle back azimuths. The negative strip east of the Snake River plain may again be associated with the continental margin at the southern Canadian coast.

[30] The geometrical spreading map (Figure 8c) shows little distance dependence. Instead, an anticorrelation between the phase velocity and the geometrical spreading is observed. For example, on the velocity map the high-velocity west coast of the United States and the north of the Snake River plain are associated with the negative geometrical spreading while much of the Basin and Range province is dominated by positive geometrical spreading. Such anticorrelation may be due to the focusing and defocusing of surface waves due to the change in velocity structure.

[31] A positive correlation between radiation pattern and azimuth variation is clearly observed on Figures 8b and 8d.

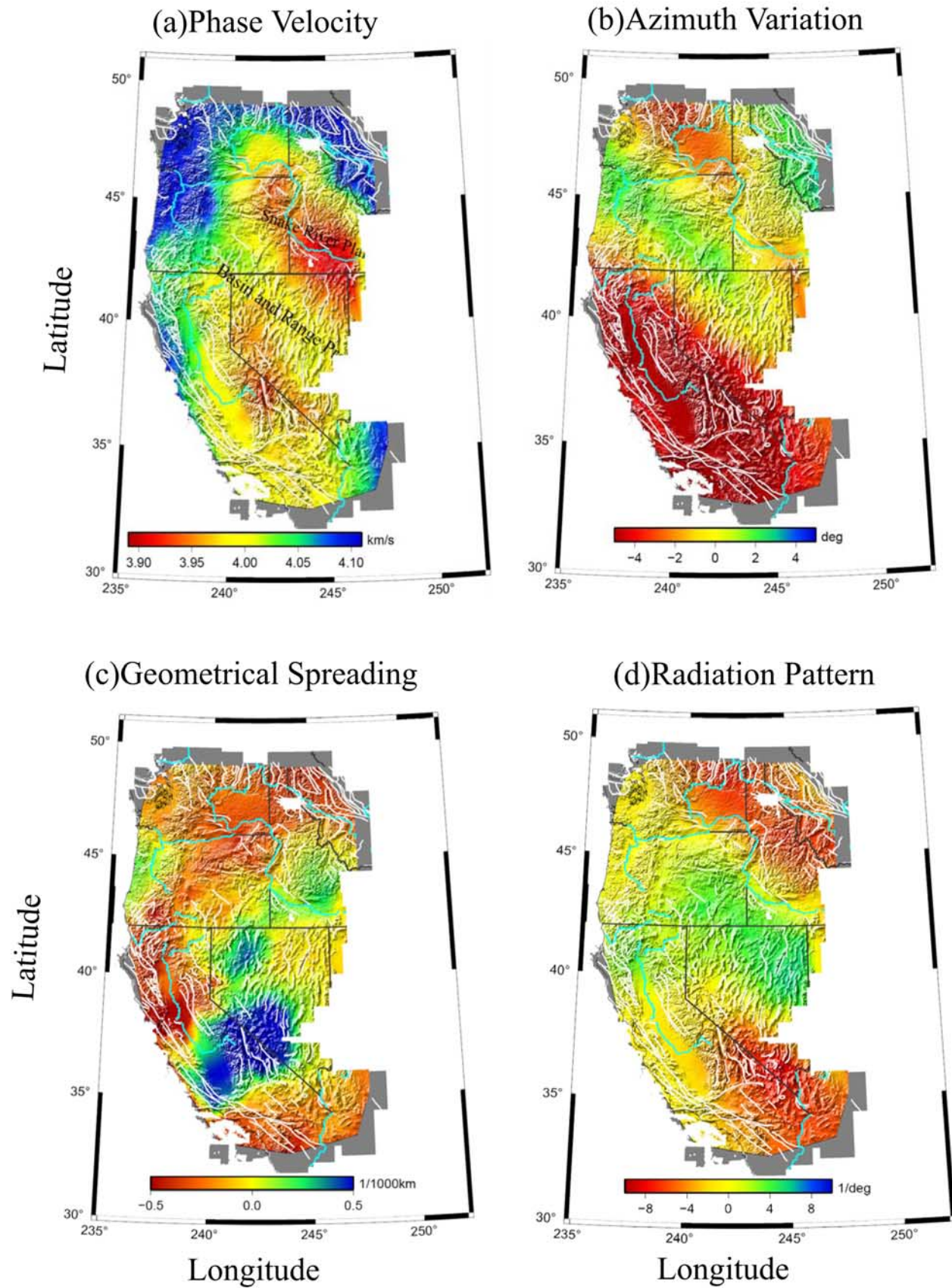


**Figure 8.** Wave parameter maps determined from the Kurile01 earthquake data, showing (a) phase velocity, (b) azimuth variations, (c) geometrical spreading, and (d) radiation pattern. Black and blue curves are state boundaries and major rivers, respectively.

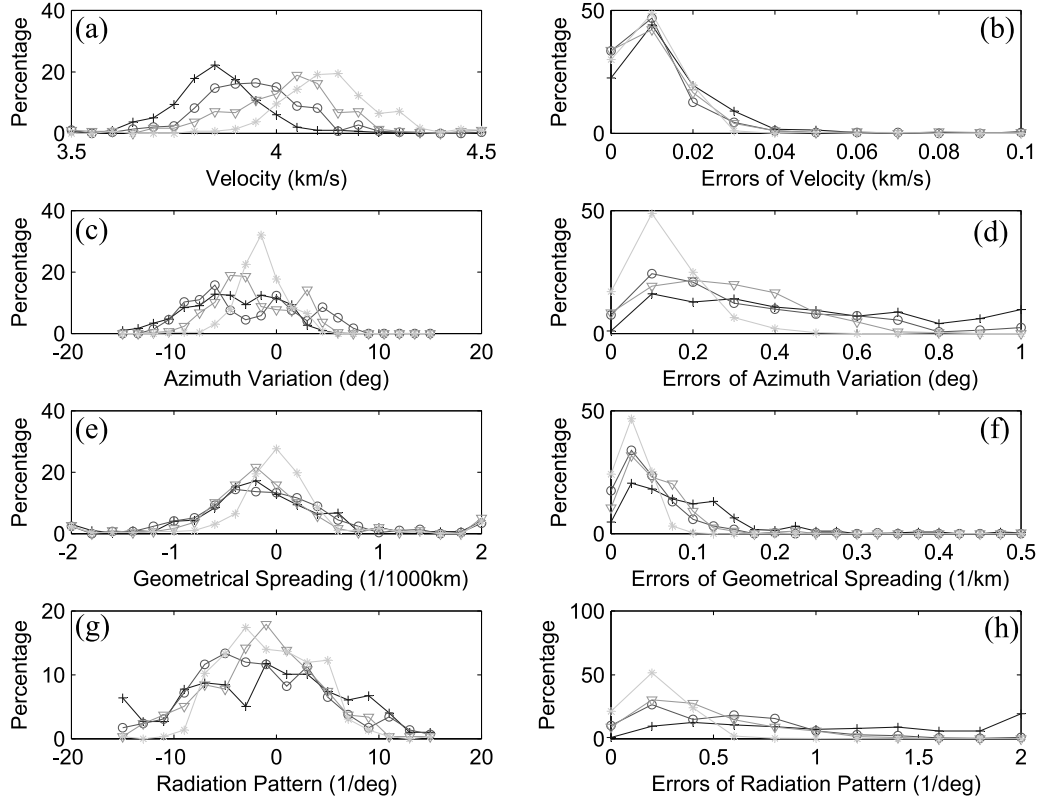


**Figure 9.** Statistics of the four wave parameters and their errors for different period bands. In each window, curves are for 60–80 s (plus), 80–100 s (circle), 100–125 s (triangle), and 125–150 s (star). The colors of the curves are progressively lighter from short to long periods.

Similar to the azimuth variations, the radiation pattern (Figure 8d) also shows strong dependency on raypaths. This suggests that the dramatic azimuthal amplitude variation may be due to the scattering along the path. The Aleutian subduction zone may also play a role in producing an azimuthal dependence in the amplitude.

[32] Amplitude variation maps in radial (geometrical spreading) and azimuthal directions (radiation pattern) are

brand new products yielded by the WG method. They may reflect a variety of wave propagation mechanism including wave focusing, defocusing, anisotropy, attenuation, and finite frequency effects. However, further theoretical and experimental studies should be conducted to find the links between amplitude variation maps and local physical properties. Together with other regional geological and geophysical observations, further analysis of these two maps may

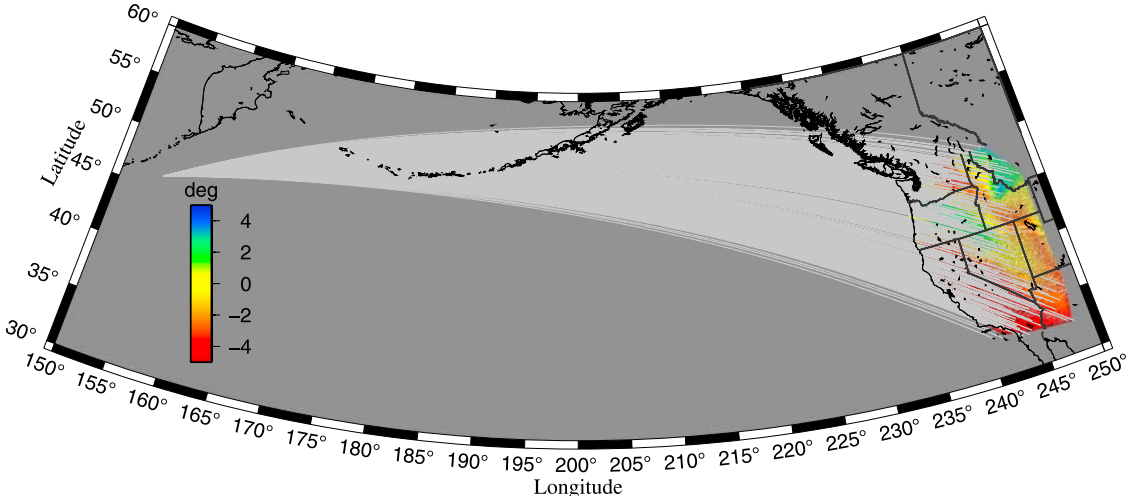


**Figure 10.** Raypaths and azimuth variations for the Kurile01 earthquake. The azimuth variation map is the same as Figure 8b.

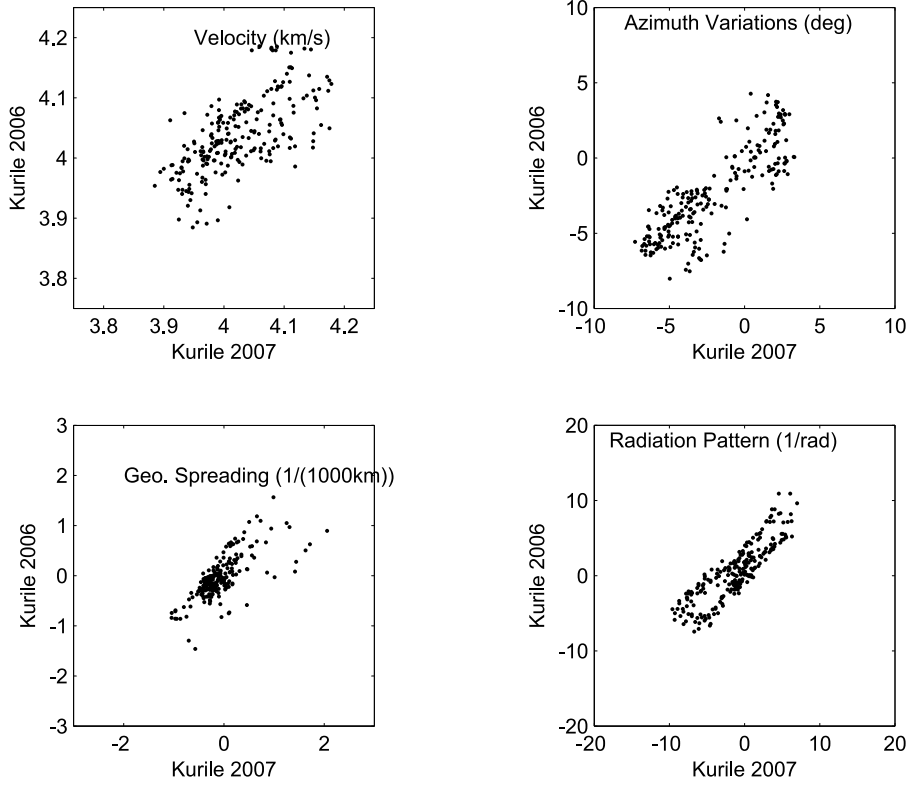


**Figure 11.** Scatterplots comparing the four parameters determined from two Kurile Islands earthquakes, showing (a) phase velocity, (b) azimuth variations, (c) geometrical spreading, and (d) radiation pattern. Horizontal and vertical components are for 13 January 2007 and 15 November 2006 earthquakes, respectively.

help us to understand the tectonic mechanism of the studied regions.

[33] We processed another earthquake from the Kurile Islands on 15 November 2006 (Kurile02 in Table 1). This earthquake is less than 100 km away from the 13 January 2007 event (Kurile01). The station coverage for the two Kurile Islands earthquakes is different due to the dynamic nature of the USAArray. The signal-to-noise ratio of the Kurile02 event is also poorer than the Kurile01 event. The results from the two earthquakes are compared via the scatterplot in Figure 11. Clearly, all four parameter maps are linearly correlated, although with some scatter. The different station coverage and different signal-to-noise ratios for two earthquakes may account for the discrepancies. The linear positive correlation suggests that the results obtained by the WG method are stable.

### 3.3. Earthquakes From Different Directions

[34] We also apply the WG method to other seven earthquakes from different directions (Table 1 and Figure 5). Figure 12 shows the four parameter maps determined from the Solomon earthquake on 1 April 2007. General patterns of the phase velocity (Figure 12a) and geometrical spreading (Figure 12c) maps are similar to the corresponding parameter maps from the Kurile Islands earthquakes shown in Figure 8. For example, both Figures 8c and 12c show strong positive geometrical spreading in much of the Basin and Range province while negative geometrical spreading along the west coast of the United States and north of Snake

River plain. At the same time, both azimuth and radiation pattern show strong dependence on raypaths. One of the major differences on the velocity maps for the two earthquakes is the dominant low velocity along the Snake River plain on Figure 8a compared to the average velocity on Figure 12a.

[35] Different station coverage and different noise level for two earthquakes are two of possible sources for the differences between two sets of results. The structure along raypaths outside of the study region may also contribute to the discrepancy. In addition, the anisotropic characteristics of medium within a subarray may also result in velocity variations for earthquakes from different directions.

[36] Effects due to these factors may be eliminated by averaging velocity maps computed from earthquakes from different directions. In Figures 13a–13d, we plot the averaged phase velocity maps of eight earthquakes (excluding Kurile02 in Table 1) for four period bands: 60–80 s, 80–100 s, 100–125 s, and 125–150 s, respectively. The general patterns are consistent for different periods: high velocity west coast and north-northeast of the Snake River plain and low-velocity Basin and Range province, while the Snake River plain appears to be a primary tectonic boundary. Substantial variations are also observed though. The high-velocity belt along the west coast is much wider for the 125–150 s than other period bands. These differences may reflect the varying depth sensitivity for different periods. The maps for different periods can be potentially inverted

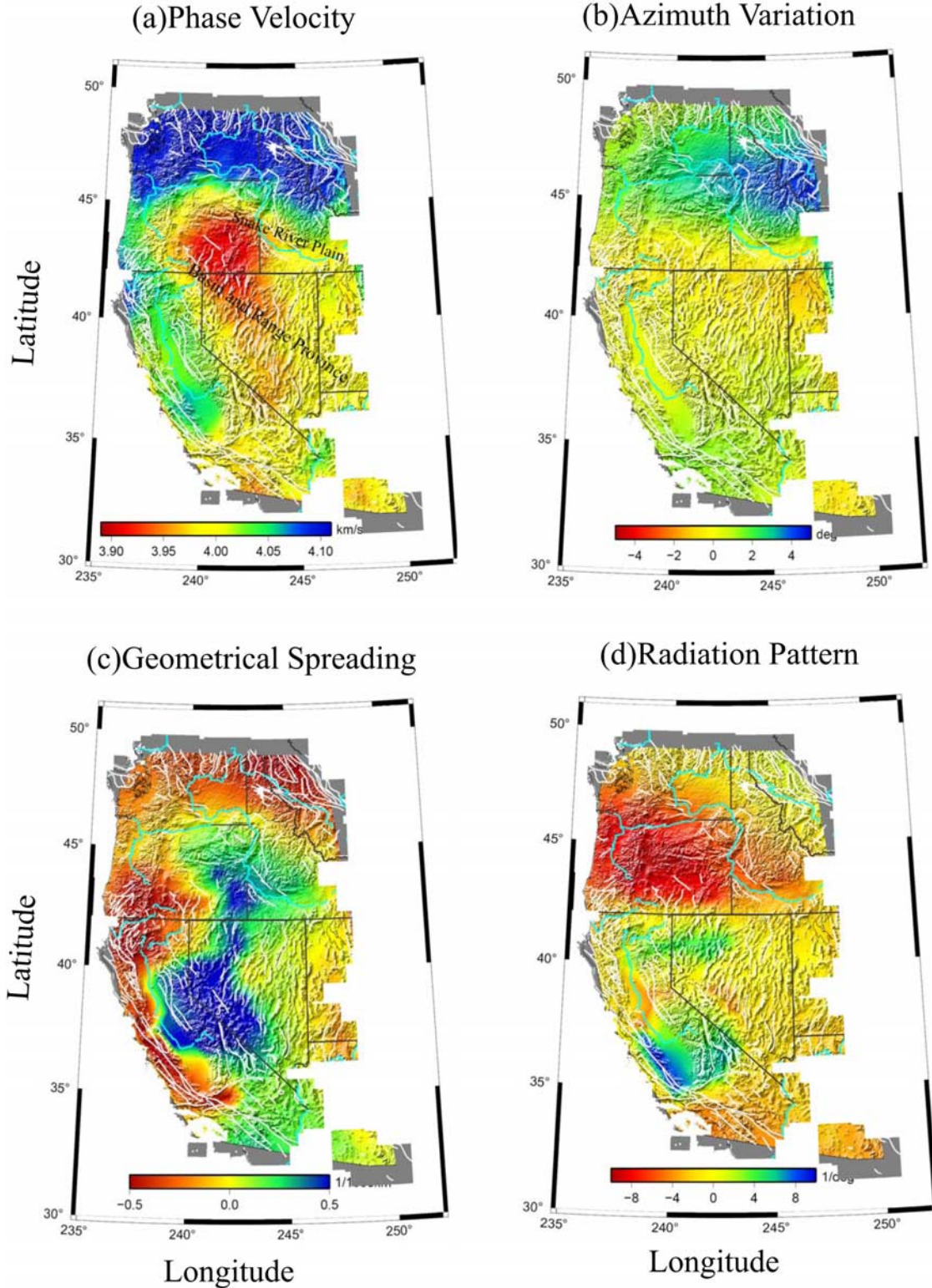


**Figure 12.** WG results for Solomon earthquake. Same scheme as Figure 8.

for a 3-D velocity model for the region covered by arrays [Liang and Langston, 2008b].

#### 4. Discussion

[37] One of our major concerns about wave gradiometry (WG) is how results are sensitive to ambient noise. One way

to investigate this is to do a random noise test. First we added random ambient noise to the original waveforms through a random time series (uniform distribution) with amplitudes between  $\pm 10\%$  of the largest amplitude of the corresponding original waveform and then applied the WG method to the new data set. The results are compared via a scatterplot in Figure 14. Very strong positive correlations

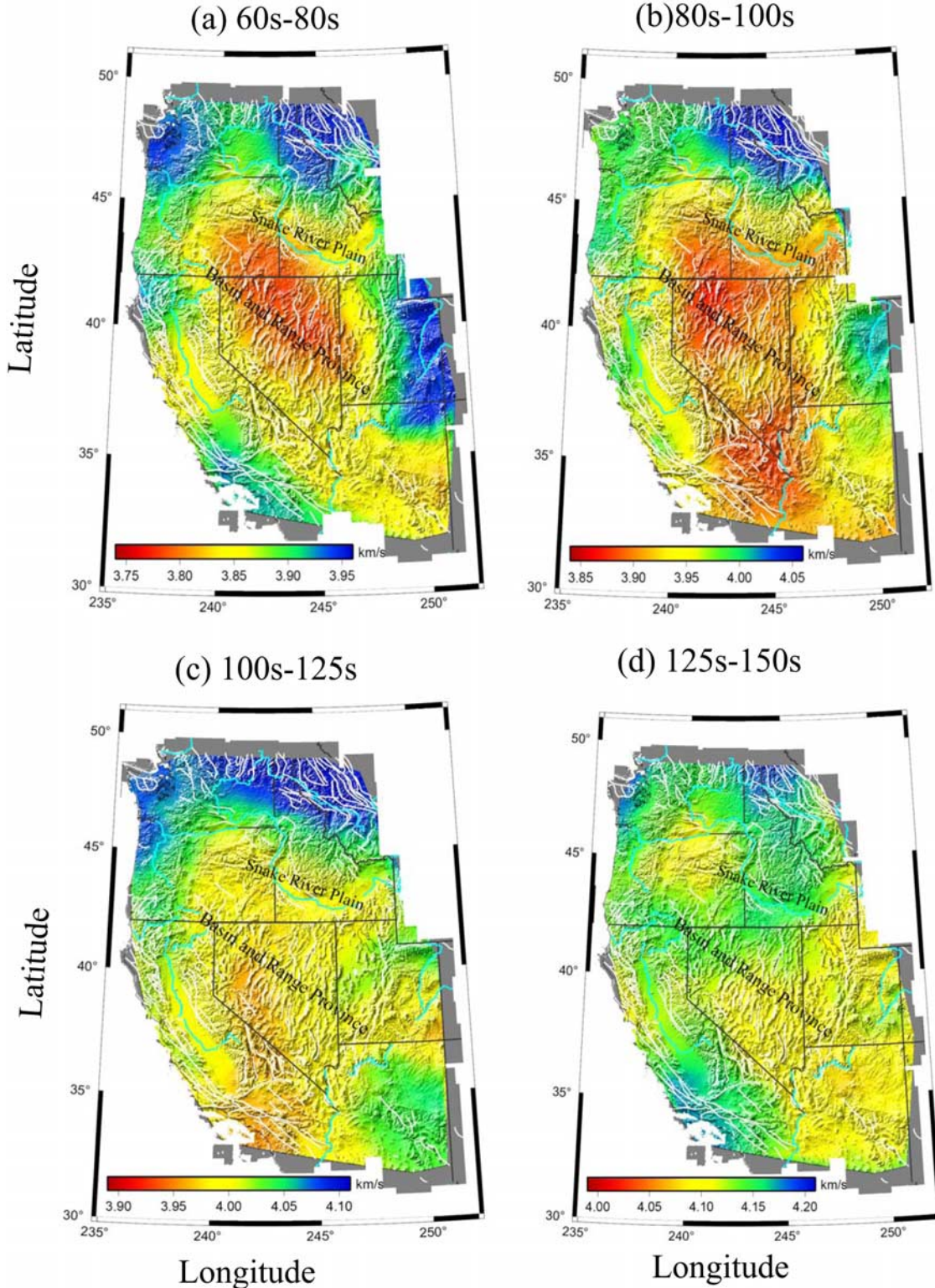


**Figure 13.** Averaged phase velocity maps for four period bands. For each period band, phase velocity maps from eight earthquakes (all in Table 1 except for the Kurile02) are averaged. General features are that the Basin and Range Province has lower velocity than the west coast of the United States. The Snake River appears to be a sharp boundary between velocity lows and highs.

are observed for all four parameters determined by data sets with and without adding noise. The standard deviation of the errors are 0.04 km/s,  $0.56^\circ$ ,  $0.2/(1000 \text{ km})$  and  $1.06/\text{rad}$ , respectively. The four parameters maps are very close to

what shown in the Figure 8. This test suggests that the WG method is stable for ambient noise (Gaussian) up to 10%.

[38] The phase velocity map of a region is traditionally obtained by inverting phase velocity along many great circle

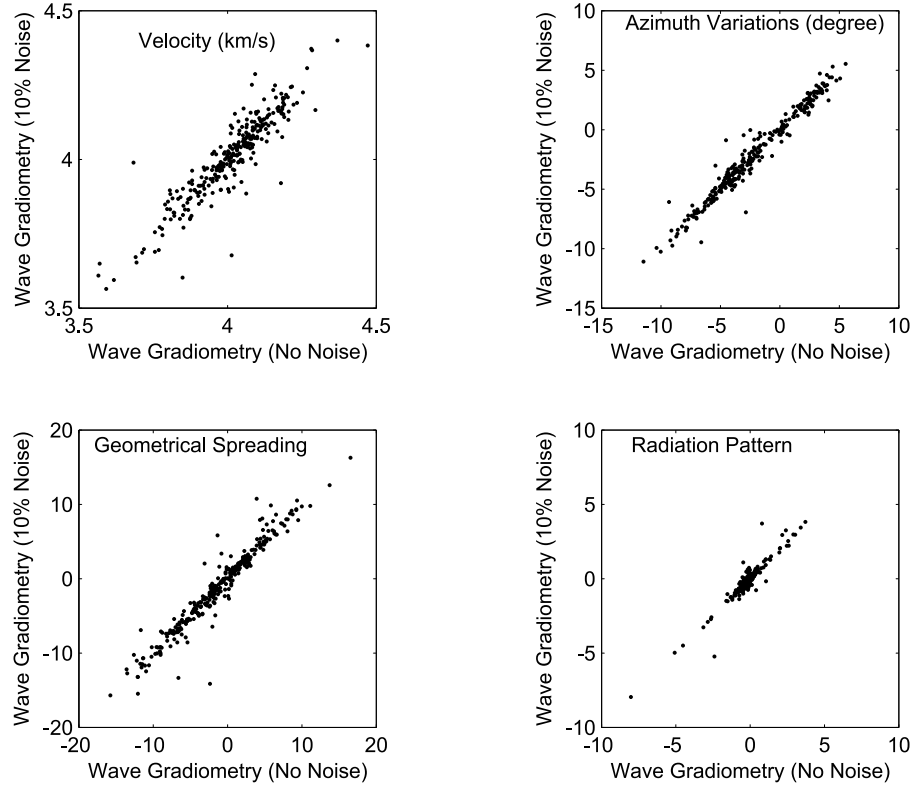


**Figure 14.** Same with the Figure 11, but comparing four parameters determined from original waveforms with and without adding 10% ambient noise. Horizontal and vertical components are for original waveforms and original waveforms plus 10% ambient noise, respectively. The data set and period band are same with what used to compute the Figure 8.

paths obtained using the single station based method [Ekström *et al.*, 1997; Laske and Masters, 1996], two station (TS) based method [Knopoff *et al.*, 1966; Yao *et al.*, 2006], or two plane wave method [Forsyth and Li, 2005; Yang and Ritzwoller, 2008]. All these methods have advantages and disadvantages. For example, the single station based method works better than other methods to find global phase velocity models but it generally needs accurate knowledge of the source which may not be available. The two station method can work for arrays with any station spacing but it requires that two stations be aligned along the great circle path. The two plane wave method solves both wave directions and phase velocity but it still needs paths from different directions to infer a reliable 2-D phase velocity variation. Otherwise, severe smearing along the paths will dominate the velocity maps. To meet these requirements, tens and hundreds of earthquakes are often needed to give better azimuthal coverage. For example, Yang and Ritzwoller [2008] used waveforms from 60 earthquakes to invert for phase velocity in the same study region as ours. On the other hand, the WG method used only “one” or several earthquakes to produce a phase velocity map such as Figures 8a, 18a, and 13a, 13b, 13c, and 13d. In addition, WG yields wave directionality (Figures 8b and 12b) and amplitude variations for every station (Figures 8c, 8d, 12c, and 12d) that cannot be determined from all other methods. Wave directionality can be very useful for the study of the scattering around stations and along paths. For example, the azimuth variations shown

in the Figure 10 might be used to model the geometry of the Aleutian subduction zone. Amplitude variations may be indicative of wave attenuation, reflection and transmission. However, the disadvantage of WG method is that dense seismic arrays are needed to compute spatial gradients.

[39] Since the 1960s, the beam forming (BF) method has been applied for source location, especially in nuclear detection [Birtill and Whiteway, 1965; Douglas *et al.*, 1999], and phase velocity estimation for deep Earth studies [Rost and Thomas, 2002]. The WG method has an advantage in providing information on amplitude variations that are totally lost in the BF method.

[40] We applied three methods (WG, BF, and TS) to the waveforms of the 13 January Kurile Islands earthquake to compare their performance. For the TS method, we automatically found all station pairs whose great circle azimuths different by  $5^\circ$  or less and great circle distances different by 800 km or longer. The phase velocities are then measured for all 1753 station pairs. For the BF method, similar to WG, we searched all stations within a radius of 150 km around a station to form a subarray and then applied the beam forming method to compute phase velocities and azimuths. Figure 15a shows the phase velocity distribution via histograms for the three methods. It is very interesting to see that the TS and WG methods yield an average phase velocity of about 4 km/s, which is consistent with the global average in the 100–125 s band, while the BF method yields an average phase velocity about 0.4 km/s higher than other two methods. On the other hand, as shown in the Figure

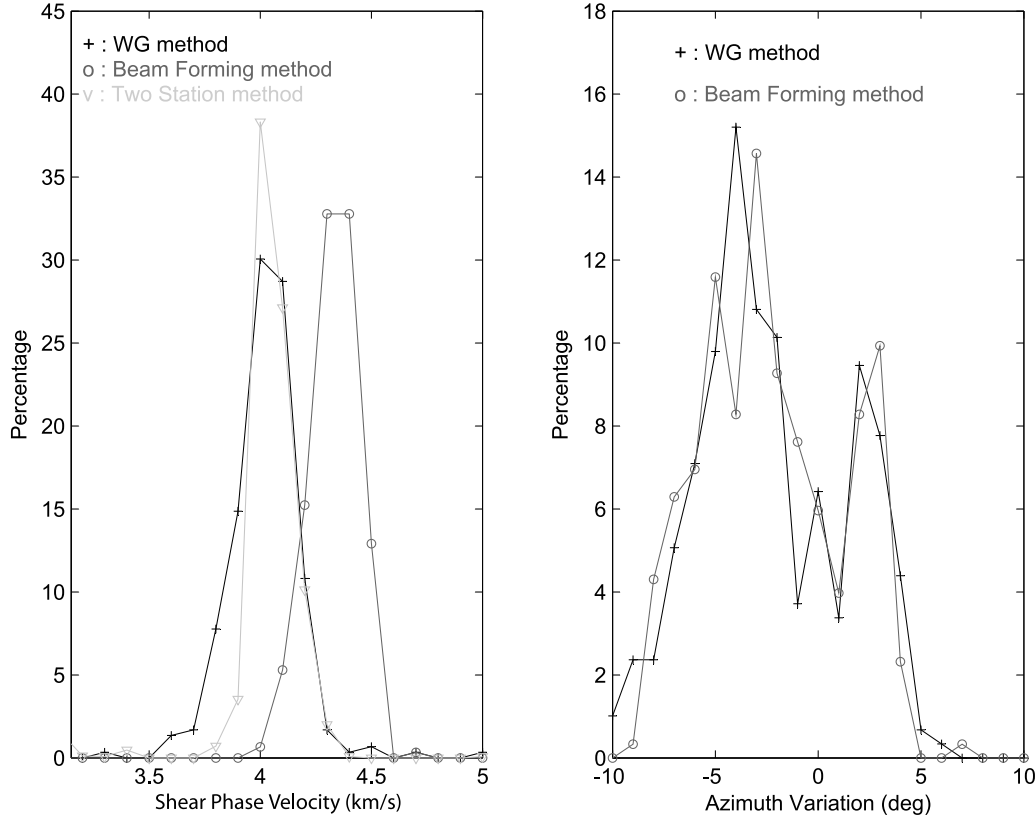


**Figure 15.** Comparison of wave gradiometry, beam forming, and two station methods. Histograms compare (a) phase velocities determined by the three methods and (b) azimuths determined from the wave gradiometry and beam forming methods. The plus, circle, and triangle mark results from wave gradiometry, beam forming, and two station methods, respectively. See text for details. The data set and period band are same as what used to compute Figure 8.

15b, the azimuths estimated from the BF and WG methods are close to each other. The scatterplot in Figure 16 shows the strong positive correlation of phase velocities and azimuths determined by two methods, although, velocities determined by the BF method are systematically higher than that determined by the WG method.

[41] We did another group of tests using Gaussian waves to compare BF and WG methods in different period bands.

For phase velocity, we found that the WG method yielded a better estimation than the BF method when the wavelengths are longer than a quarter of the array diameter. Otherwise, the BF method yields better results. In the case with an array diameter of about 300 km and an average velocity of 4 km/s, the WG method will give better velocity estimation than BF for periods longer than 20 s. The same trend is observed for azimuth estimation, even though the azimuth errors are

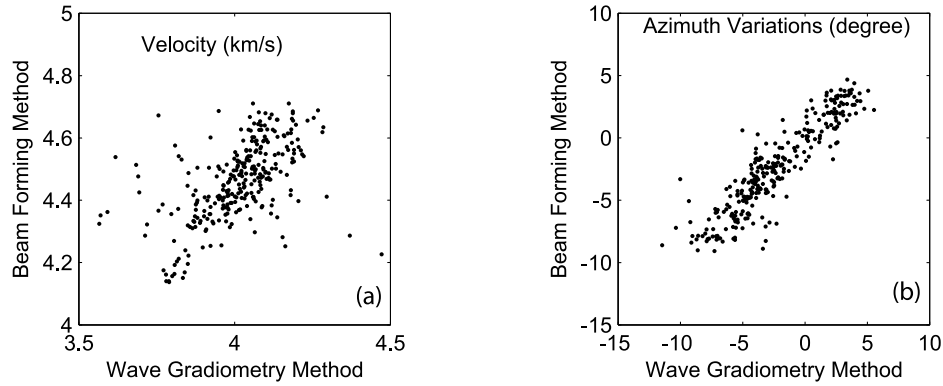


**Figure 16.** Scatterplot to compare (a) phase velocities and (b) azimuths determined by the wave gradiometry (horizontal) and beam forming (vertical). The data set and period band are same with what used to compute the Figure 8.

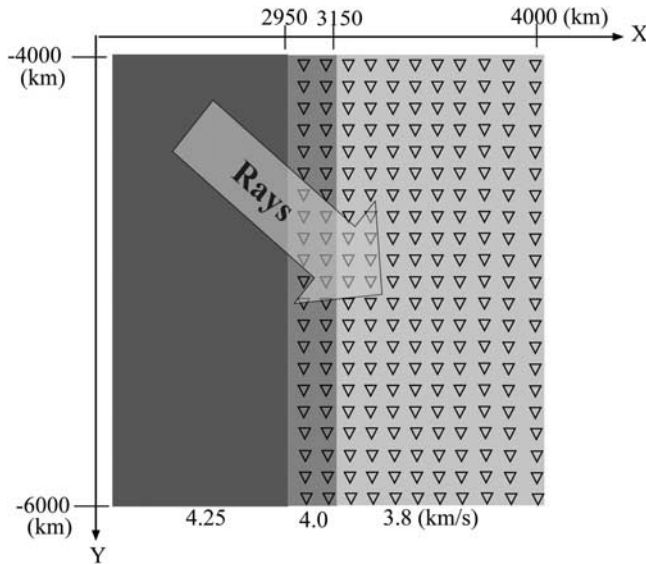


**Figure 17.** Numerical experiment to simulate the Kurile island earthquake recorded by USArray. Three distinct regimes from west to east are used to mimic the lithosphere of the Pacific Ocean, the west coast of the United States, and the Basin and Range province, respectively. The array has a uniform grid spacing of 100 km. The geometry of the array and the wave directions and distances are set to mimic the waves from the Kurile Islands event propagating across USArray.

generally small for both methods for all period bands. However, the WG method is computationally much faster than the BF method.

[42] The capability of WG is strongly dependent on the accuracy of the spatial gradient computation that is a function of the wave number (frequency over phase velocity) and station spacing as well as the angle between the receiver pairs and the raypath ( $d\theta$ ). The errors in spatial gradients are smaller for smaller wave number and smaller array spacing. In this study, two methods are introduced to account for errors. The reducing velocity method is used to intentionally decrease the wave number. The weighted inversion method makes the method workable for an array in any geometry and also to account for Taylor series truncation errors.

[43] To summarize, phase velocities estimated by WG and TS methods are consistent with each other while the BF method systematically overestimates the phase velocity in period bands longer than 20 s for an array geometry like USArray. The BF and TS methods may work better for shorter periods and larger aperture arrays. As array data for different scales, such as local or regional, become increasingly available, we expect all three techniques can be integrated together to take full advantage of array data sets.

[44] As shown in Figures 8b, 10, and 12b, azimuth variations determined by wave gradiometry are the accumulated wave directionality changes along the whole raypath. The radiation pattern (Figures 8d and 12d), i.e., the amplitude variation in the azimuthal direction, also shows strong dependency on raypaths. We performed a numerical

experiment to investigate how the raypaths affect the results from WG.

[45] For this experiment, the source is located at (0,0,0) and the experiment geometry is plotted as the grid in Figure 17. The array has a uniform station spacing of 100 km and spans 3000–4000 km in the  $x$  direction and –6000 to –4000 km in the  $y$  direction. The 2-D space is divided into three provinces with velocity equal to 4.25, 4.0, and 3.8 km/s to represent the lithosphere of Pacific Ocean, the west coast of the United States, and the Basin and Range Province, respectively. However, only the later two provinces are covered by the array. The belt in the middle is 200 km wide. The geometry and model are chosen to simulate Rayleigh waves from the Kurile Islands earthquakes propagating across the Pacific Ocean and the western United States. The Gaussian function (23) is used to produce waves at each receiver:

$$u(t, x, y) = \frac{-\sin(2\theta)}{\sqrt{x^2 + y^2}} \exp[-0.0005(t - xp_x - yp_y)] \quad (23)$$

The wave path from source to receive is based on optic ray theory which is valid under the infinite frequency assumption.

[46] Following the same process as in the real data processing, we generate the four output maps shown in Figure 18. The phase velocity in Figure 18a shows that the two distinct provinces covered by the array can be well resolved, even though the width of the high velocity belt is only about half of the wavelength of 400 km. This experiment also shows that the long raypaths in the high velocity region (4.25 km/s) have little influence on the phase velocities determined by the WG method. Therefore we can conclude that phase velocities from the WG method represent the local average around the master station. The resolution is about the subarray diameter, 200 km in this case. However, as mentioned before, this experiment is based on ray theory which is valid only at high frequency, further experiments are necessary to investigate how finite frequency wave scattering effects affect the WG results.

[47] The azimuth variations,  $\delta\theta$ , in Figure 18b are exclusively negative, that is, the computed azimuths are all smaller than the azimuths of straight lines connecting the source and receivers. Negative azimuth variations are due to the refraction at the two tectonic boundaries at 2950 km and 3150 km across which waves propagate from high velocity to low velocity. Also note that the azimuth variations become smaller toward the northeast corner because the incident angles of rays are increasingly larger toward that direction. The azimuth variation should be zero if the ray is vertically incident across a boundary ( $\delta\theta = 90^\circ$ ). The absolute azimuth variations are between  $5^\circ$  and  $10^\circ$  which are similar to the negative azimuth variations determined from 13 January 2007 Kurile Islands earthquake in the period band 100–125 s (refer to the first peak of the triangular-marked curve in Figure 9c). This suggests that a velocity contrast of 0.25 km/s along the oceanic and continental lithosphere boundary is enough to account for the azimuth anomaly.

[48] The geometrical spreading,  $A_r$  (Figure 18c), although very small, is consistently decreasing as the ray lengths

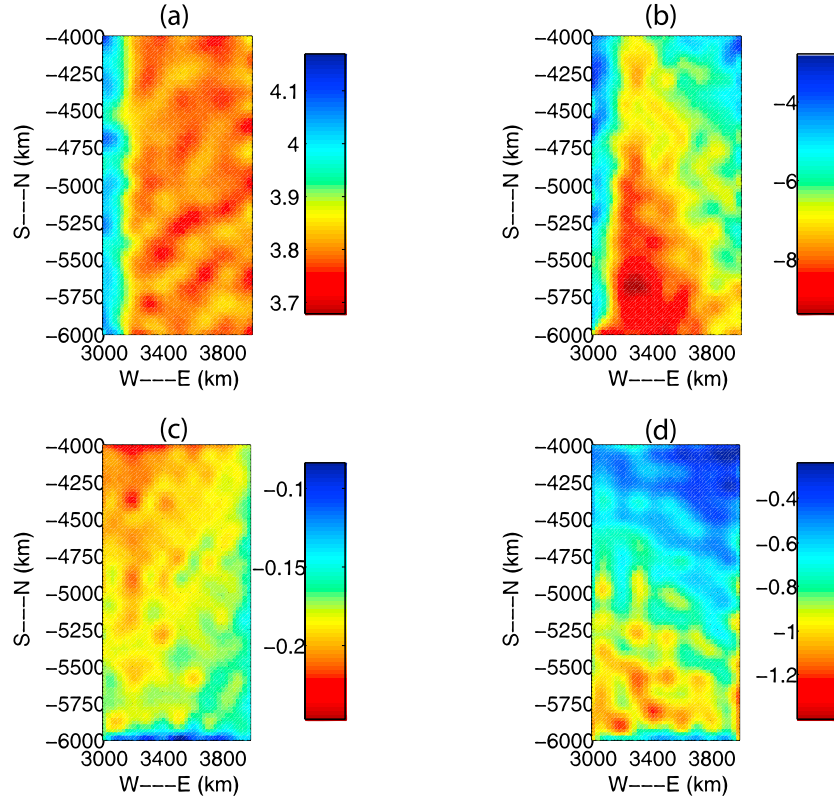


**Figure 18.** Four WG parameters determined from the numerical experiment shown in the Figure 17, showing (a) phase velocity, (b) azimuth variations, (c) geometrical spreading, and (d) radiation pattern.

increase from northwest to the southeast. This is consistent with the wave model used to synthesize the waves. However, the real data observations of  $A_r$  in Figures 8c and 12c shows little distance dependence. This may be due to the fact that focusing and defocusing of waves by local structure have larger effects on amplitude variation than distance. Similar to the real data results, the radiation pattern  $A_\theta$  in Figure 18d indeed shows a strong dependence on the ray direction. The amplitude of the radiation pattern decreases toward the northeast. This is also consistent with the wave model which gives  $A_\theta = \frac{\partial G}{\partial \theta} = \frac{2 \cos(2\theta)}{\sin(2\theta)}$  by applying equation (6) to equation (23) with  $G = \frac{\sin(2\theta)}{\sqrt{x^2+y^2}}$ .

## 5. Conclusion

[49] Wave gradiometry is a new array data processing technique that can be used to extract phase velocity  $v$ , azimuth variation  $\delta\theta$ , geometrical spreading  $A_r$ , and radiation pattern  $A_\theta$  from spatial gradients of waveforms using equations (4) to (8). Spatial gradients are computed using a weighted inversion method for irregular arrays. The errors of the spatial gradient computation are linearly related to the wave number and station spacing as well as the angle between the receiver pairs and the raypath. The reducing velocity method and weighted inversion method are introduced to account for errors.

[50] The stability of this method is addressed by two tests. The first test shows strong similarity between the WG parameters from different earthquakes. The second test shows that the WG results are quite stable for ambient

noise level as high as 10% of the peak amplitude of the original waveforms.

[51] Numerical experiments are conducted to test the theory and techniques to compute spatial gradients. Numerical experiments are also done to help explain the parameters determined from the WG method. The phase velocity maps determined from the two Kurile island earthquakes (Figure 8), the Solomon earthquake (Figure 12), and the average of eight earthquakes (Figure 13) show dominant low velocities for the Basin and Range province versus dominant high velocities for the west coast and north and northeast of the Snake River. The Snake River plain appears as a primary tectonic boundary for all period bands between 60 s and 150 s. Consistent with the numerical experiments, both azimuth variation and radiation pattern show strong dependence on raypath. A velocity contrast of 0.25 km/s across the ocean-continent lithospheric boundary is needed to explain the negative azimuth variations of all rays south of the Aleutian subduction zone in Figure 10. Geometrical spreading patterns may reflect local wave amplitude changes due to focusing and defocusing in heterogeneous structure.

[52] There are many sources that may contribute to errors in the WG results, including station coverage, ambient noise, and the structure along raypaths outside of the study region. In addition, the anisotropic characteristics of medium within a subarray may also result in velocity variations for earthquakes from different directions.

[53] Wave gradiometry can determine other wave parameters in addition to phase velocity such as wave direc-

ality and amplitude variations. The beam forming method does not determine amplitude variations while the two station method does not give both wave directionality and amplitude variation. The WG method is also computationally more efficient than the other two methods.

[54] Further studies are needed to test this technique in different situations. Investigations are needed to understand amplitude variations and their physical meaning. Using earthquakes from different directions to study the anisotropic structure is also a new direction worth further exploring. The numerical experiments conducted in this study are based on the ray theory. More experiments may be necessary to test how the WG results will be affected by the finite frequency effects, especially when the subarray used is smaller than the half wavelength of waves.

[55] **Acknowledgments.** We thank the associated editor Jeroen Ritsema and the two reviewers for their constructive comments and suggests for improving this work. This work is supported by the Center for Earthquake Research and Information (CERI).

## References

- Armstrong, R. L., W. P. Leeman, and H. E. Malde (1975), K-ar dating quaternary and neogene volcanic rocks of the Snake River plain, Idaho, *Am. J. Sci.*, 275, 225–251.
- Barmin, M. P., H. Ritzwoller, and A. L. Levshin (2001), A fast reliable method for surface wave tomography, *Pure Appl. Geophys.*, 158, 1351–1375, doi:10.1007/PL00001225.
- Bedle, H., and S. van der Lee (2007), Upper mantle S-velocity variance beneath North America, *Eos Trans. AGU*, 88(52), Fall Meet. Suppl., Abstract S41B-0562.
- Beghein, C., J. A. Snock, and M. J. Fouch (2007), Inferences on upper mantle seismic velocity and anisotropy in western North America from surface wave analyses, *Eos Trans. AGU*, 88(52), Fall Meet. Suppl., Abstract S43D-05.
- Birtill, J. W., and F. E. Whiteway (1965), The application of phased arrays to analysis of seismic body waves, *Philos. Trans. R. Soc. London, Ser. A*, 258, 421–493, doi:10.1098/rsta.1965.0048.
- CERI Array Working Group (2007), Wave gradiometry with a refraction seismograph, paper presented at Annual Meeting 2007, Seismol. Soc. Am, El Cerrito, Calif.
- Dahlen, F. A., and J. Tromp (1998), *Theoretical Global Seismology*, Princeton Univ. Press, Princeton, NJ.
- Douglas, A., O. D. Marshall, J. B. Young, D. Porter, and N. J. Wallis (1999), Putting nuclear-test monitoring to the test, *Nature*, 398, 474–475, doi:10.1038/19000.
- Dziewonski, A. M., and D. L. Anderson (1981), Preliminary reference earth model, *Phys. Earth Planet. Inter.*, 25, 297–356, doi:10.1016/0031-9201(81)90046-7.
- Ekstrom, G., J. Tromp, and E. Larson (1997), Measurements and global models of surface wave propagation, *J. Geophys. Res.*, 102, 8137–8157, doi:10.1029/96JB03729.
- Forsyth, D. W., and A. Li (2005), Array analysis of two-dimensional variations in surface wave phase velocity and azimuthal anisotropy in the presence of multipathing interference, in *Seismic Earth: Array Analysis of Broadband Seismograms*, *Geophys. Monogr. Ser.*, vol. 157, edited by A. Levander and G. Nolet, pp. 81–97, AGU, Washington, D.C.
- Hearn, T. M. (1996), Anisotropic pn tomography in the western united states, *J. Geophys. Res.*, 101(B4), 8403–8414, doi:10.1029/96JB00114.
- Herrmann, R. B. (1973), Some aspects of band-pass filtering of surface waves, *Bull. Seismol. Soc. Am.*, 63(2), 663–671.
- Knopoff, L., S. Muller, and W. L. Pilant (1966), Structure of the crust and upper mantle in the Alps from the phase velocity of Rayleigh waves, *Bull. Seismol. Soc. Am.*, 56, 1009–1044.
- Langston, C. A. (2007a), Spatial gradient analysis for linear seismic arrays, *Bull. Seismol. Soc. Am.*, 97(1B), 265–280, doi:10.1785/0120060100.
- Langston, C. A. (2007b), Wave gradiometry in two dimensions, *Bull. Seismol. Soc. Am.*, 97(2), 401–416, doi:10.1785/0120060138.
- Langston, C. A. (2007c), Wave gradiometry in the time domain, *Bull. Seismol. Soc. Am.*, 97(3), 926–933, doi:10.1785/0120060152.
- Langston, C. A., and C. Liang (2008), Gradiometry for polarized seismic waves, *J. Geophys. Res.*, 113, B08305, doi:10.1029/2007JB005486.
- Langston, C. A., P. Bodin, C. Powell, M. Withers, S. Horton, and W. Mooney (2006), Explosion source strong ground motion in the Mississippi embayment, *Bull. Seismol. Soc. Am.*, 96, 1038–1054, doi:10.1785/0120050105.
- Laske, G., and G. Masters (1996), Constraints on global phase velocity maps from long-period polarization data, *J. Geophys. Res.*, 101, 16,059–16,075, doi:10.1029/96JB00526.
- Levander, A., F. Niu, M. S. Miller, Y. Zhai, and K. Liu (2007), USAArray receiver function images of the lithosphere in the western U. S., *Eos Trans. AGU*, 88(52), Fall Meet. Suppl., Abstract S44B-01.
- Liang, C., and C. A. Langston (2008a), Ambient seismic noise tomography and structure of eastern North America, *J. Geophys. Res.*, 113, B03309, doi:10.1029/2007JB005350.
- Liang, C., and C. A. Langston (2008b), Three-dimensional crustal structure of eastern North America extracted from ambient noise, *J. Geophys. Res.*, doi:10.1029/2008JB005919, in press.
- Lin, F., M. P. Moschetti, and M. H. Ritzwoller (2008), Surface wave tomography of the western United States from ambient seismic noise: Rayleigh and Love wave phase velocity maps, *Geophys. J. Int.*, 173, 281–298, doi:10.1111/j.1365-246X.2008.03720.x.
- Moschetti, M. P., and M. Ritzwoller (2007), Surface wave tomography of the western United States from ambient seismic noise: Rayleigh wave group velocity maps, *Geochem. Geophys. Geosyst.*, 8, Q08010, doi:10.1029/2007GC001655.
- Rost, S., and T. Thomas (2002), Array seismology; methods and applications, *Rev. Geophys.*, 40(3), 1008, doi:10.1029/2000RG000100.
- Saltzer, R. L., and E. D. Humphreys (1997), Upper mantle p wave velocity structure of the eastern snake river plain and its relationship to geodynamic models of the region, *J. Geophys. Res.*, 102(B6), 11,829–11,841, doi:10.1029/97JB00211.
- Sigloch, K., and G. Nolet (2007), Global p-wave tomography using finite-frequency modeling and finite-frequency data, *Eos Trans. AGU*, 88(52), Fall Meet. Suppl., Abstract S31E-06.
- Spudich, P., L. K. Steck, M. Hellweg, J. B. Fletcher, and L. M. Baker (1995), Transient stresses at Parkfield, California produced by the m7.4 Landers earthquake of June 28, 1992: Observations from the upsr dense seismograph array, *J. Geophys. Res.*, 100, 675–690, doi:10.1029/94JB02477.
- van der Lee, S., and A. Frederiksen (2005), Surface wave tomography applied to the North American upper mantle, in *Seismic Earth: Array Analysis of Broadband Seismograms*, *Geophys. Monogr. Ser.*, vol. 157, edited by A. Levander and G. Nolet, pp. 67–80, AGU, Washington, D.C.
- van der Lee, S., and G. Nolet (1997), Upper mantle s velocity structure of north America, *J. Geophys. Res.*, 102, 22,815–22,838, doi:10.1029/97JB01168.
- West, J. D. (2007), Shear-wave splitting in the great basin, *Eos Trans. AGU*, 88(52), Fall Meet. Suppl., Abstract S41B-0556.
- Yang, Y., and M. Ritzwoller (2008), Teleseismic surface wave tomography in the western us using the transportable array component of USAArray, *Geophys. Res. Lett.*, 35, L04308, doi:10.1029/2007GL032278.
- Yao, H., R. D. van der Hilst, and M. V. de Hoop (2006), Surface-wave array tomography in SE Tibet from ambient seismic noise and two-station analysis – I. Phase velocity maps, *Geophys. J. Int.*, 166, 732–744, doi:10.1111/j.1365-246X.2006.03028.x.

C. A. Langston and C. Liang, Center for Earthquake Research and Information, University of Memphis, 3876 Central Avenue, Memphis, TN 38152, USA. (clangstn@memphis.edu; liangseis@gmail.com)